MATERIALS SCIENCE

Sub-angstrom noninvasive imaging of atomic arrangement in 2D hybrid perovskites

Mykola Telychko[1]†, Shayan Edalatmanesh[2,3]†, Kai Leng[4]†, Ibrahim Abdelwahab[1,5], Na Guo[6], Chun Zhang[6], Jesús I. Mendieta-Moreno[2], Matyas Nachtigall[2], Jing Li[5], Kian Ping Loh[1]*, Pavel Jelínek[2,3]*, Jiong Lu[1,5]*

Noninvasive imaging of the atomic arrangement in two-dimensional (2D) Ruddlesden-Popper hybrid perovskites (RPPs) is challenging because of the insulating nature and softness of the organic layers. Here, we demonstrate a sub-angstrom resolution imaging of both soft organic layers and inorganic framework in a prototypical 2D lead-halide RPP crystal via combined tip-functionalized scanning tunneling microscopy (STM) and noncontact atomic force microscopy (ncAFM) corroborated by theoretical simulations. STM measurements unveil the atomic reconstruction of the inorganic lead-halide lattice and overall twin-domain composition of the RPP crystal, while ncAFM measurements with a CO-tip enable nonperturbative visualization of the cooperative reordering of surface organic cations driven by their hydrogen bonding interactions with the inorganic lattice. Moreover, such a joint technique also allows for the atomic-scale imaging of the electrostatic potential variation across the twin-domain walls, revealing alternating quasi-1D electron and hole channels at neighboring twin boundaries, which may influence in-plane exciton transport and dissociation.

INTRODUCTION

The two-dimensional (2D) Ruddlesden-Popper hybrid perovskites (RPPs) offer a remarkably rich material platform for optoelectronic device applications, for which the excitonic properties are closely linked to their quantum well structures consisting of soft insulating organic layers sandwiched between conducting inorganic lead-halide frameworks. The presence of additional soft insulating organic layers in 2D RPPs versus their 3D counterparts not only introduces the two-dimensionality and the emergence of many quantum phenomena (1–4) but also leads to significantly enhanced photo and chemical stability (5, 6) and tunable optoelectronic properties of RPPs (7–11). Such unique dielectric and quantum confinement effects establish RPPs as a promising class of materials for next-generation optoelectronic applications (12–16). Furthermore, recent photoluminescence (PL) studies demonstrate that organic cations in RPPs and polarizable inorganic lattice are prone to cooperative structural relaxations under external perturbations including strain and light exposure and thus markedly alter the optoelectronic response of RPPs (17). Analogously to their 3D counterparts, the structural relaxations of the inorganic lattice of 2D RPPs may lead to the emergence of the various ferroelastic domains and twin boundaries, which have not been hitherto studied at the atomic scale either in 3D or in 2D hybrid perovskites.

Superior advantages of RPPs for a wide range of photovoltaic and optoelectronic applications are further exemplified by a number of recently uncovered phenomena related to exciton transport and recombination in these materials. For instance, the most recent experimental breakthroughs show that RPP crystals render remarkably long-range exciton diffusion (hundreds of nanometers) and reduced rates of exciton recombination (18, 19). Furthermore, it has been demonstrated that charge transport is largely determined by the intrinsic crystalline structure of the RPPs, pronounced exciton-polaronic effects (20, 21), and peculiarities of the energy landscape (22). Nevertheless, fundamental understanding of these exciton and carrier dynamics phenomena in RPP is not complete, as it requires the microscopic knowledge of the structural properties of RPPs, which remains elusive to date.

Future progress in this field hinges on the atomic-scale understanding of the dynamic structural reordering and cooperative lattice relaxation in the crystal that impact their electronic, optoelectronic, and excitonic properties. Therefore, real-space noninvasive atomic imaging of both top organic layers and the underlying inorganic lattice in a 3D fashion is highly desired. Unfortunately, the insulating nature and softness of organic layers as well as the "buried" inorganic framework render atomically resolved imaging of the RPPs a grand challenge, beyond the capabilities of the current state-of-the-art imaging techniques including both scanning tunneling microscopy (STM) and scanning transmission electron microscopy (STEM). Although tunneling through insulating organic layers can be exploited to resolve the atomic lattice of inorganic framework via STM, the soft organic chains can be easily excited via an inelastic tunneling process, leading to their relocation and the disordering of the organic layer. Alternatively, beam-efficient STEM imaging techniques have been developed to image inorganic lattices of the 3D organic-inorganic perovskites (23–25). However, the application of STEM to image 2D organic-inorganic RPPs causes the structural damage to such beam-sensitive RPPs due to the collisions of the soft organic layers with the energetic electron beam (26).

Recent advances in tuning fork (qPlus)–based noncontact atomic force microscopy (ncAFM) imaging with a carbon monoxide (CO)–functionalized tip have established this technique as a powerful tool

[1]Department of Chemistry, National University of Singapore, 3 Science Drive 3, Singapore 117543, Singapore. [2]Institute of Physics, The Czech Academy of Sciences, 162 00 Prague, Czech Republic. [3]Regional Centre of Advanced Technologies and Materials, Palacký University, 78371 Olomouc, Czech Republic. [4]Department of Applied Physics, The Hong Kong Polytechnic University, Hung Hom, Kowloon, Hong Kong, China. [5]Centre for Advanced 2D Materials (CA2DM), National University of Singapore, 6 Science Drive 2, Singapore 117546, Singapore. [6]Department of Physics, National University of Singapore, Blk S12, Science Drive 3, Singapore 117551, Singapore.
*Corresponding author. Email: chmluj@nus.edu.sg (J.L.); pavel.jelinek@fzu.cz (P.J.); chmlohkp@nus.edu.sg (K.P.L.).
†These authors contributed equally to this work.

for atomically resolved studies (*27*). It has been demonstrated that ncAFM with a judiciously decorated tip offers extraordinary sub-angstrom resolution imaging (<1 Å) of solid surfaces (*28*), organic materials (*29–31*), and even nonperturbative imaging of weakly bonded systems such as water clusters (*32, 33*). Therefore, the qPlus-ncAFM technique potentially acts as an ideal tool for noninvasive sub-angstrom–scale imaging of insulating organic layers in RPPs. To this end, we used low-temperature STM and ncAFM imaging to resolve atomic structures of both inorganic framework and organic layers in the prototypical hybrid lead-halide RPP crystal. STM imaging resolves the reconstruction of the inorganic octahedral framework and unveils the twin-domain composition of the RPPs, while ncAFM imaging with a CO-functionalized tip enables a noninvasive visualization of the cooperative reconstruction of the on-surface cations (Fig. 1A), presented by a well-ordered array of the cation pairs. The structural relaxation of the organic layers is interlocked with the deformation of the inorganic lattice through hydrogen bonding, which is corroborated by density functional theory (DFT) calculations. The lattice deformation leads to the formation of ferroelastic domains stitched via quasi-1D twin boundaries with spatial extension over hundreds of nanometers. We demonstrate the atomic-scale imaging of the electrostatic potential variation across the twin-domain walls, revealing alternating quasi-1D electron and hole channels at neighboring twin boundaries, which sheds new light on the mechanisms of the efficient separation of photoexcited electron–hole pairs and exciton transport in 2D RPPs.

RESULTS
Exfoliation of 2D RPP atomic layers for the STM measurements

We have selected the $n = 4$ homolog of the lead-iodine (Pb-I) RPP family for the combined STM/ncAFM imaging. The RPP family is described by a general chemical formula $(CH_3(CH_2)_3NH_3)_2(CH_3NH_3)_{n-1}Pb_nI_{3n+1}$, where n reflects the number of inorganic octahedral sheets (typically $n = 1$ to 4) sandwiched by butylammonium $(CH_3(CH_2)_3NH_3)$ cations (denoted as BA^+). In analogy to the 3D counterpart, the inorganic RPP framework consists of the corner-sharing $[PbI_6]$ octahedral cages. Furthermore, short polar methyl-ammonium (CH_3NH_3) (denoted as MA^+) molecules reside in the intraoctahedral space to balance the negative electrostatic charge of the $[PbI]^-$ lattice. The presence of insulating BA^+ cations in the RPPs significantly reduces its out-of-plane conductivity and precludes STM study of bulk samples.

To overcome this issue, we mechanically exfoliated bulk $n = 4$ RPP crystals onto the Au(100) substrate to produce monolayer and few-layer flakes for a combined STM/ncAFM measurement at 4.5 K. The layer-dependent optical contrast (Fig. 1A) facilitates the tip positioning over RPP flakes with any desired thickness. The mechanical exfoliation generally produces BA^+-terminated single-crystal flakes.

A representative STM image of a few-layered RPP flake acquired at positive sample bias voltages (V_s) reveals a periodic dimer-like pattern (Fig. 1B). Such a dimer-like STM reconstruction strongly
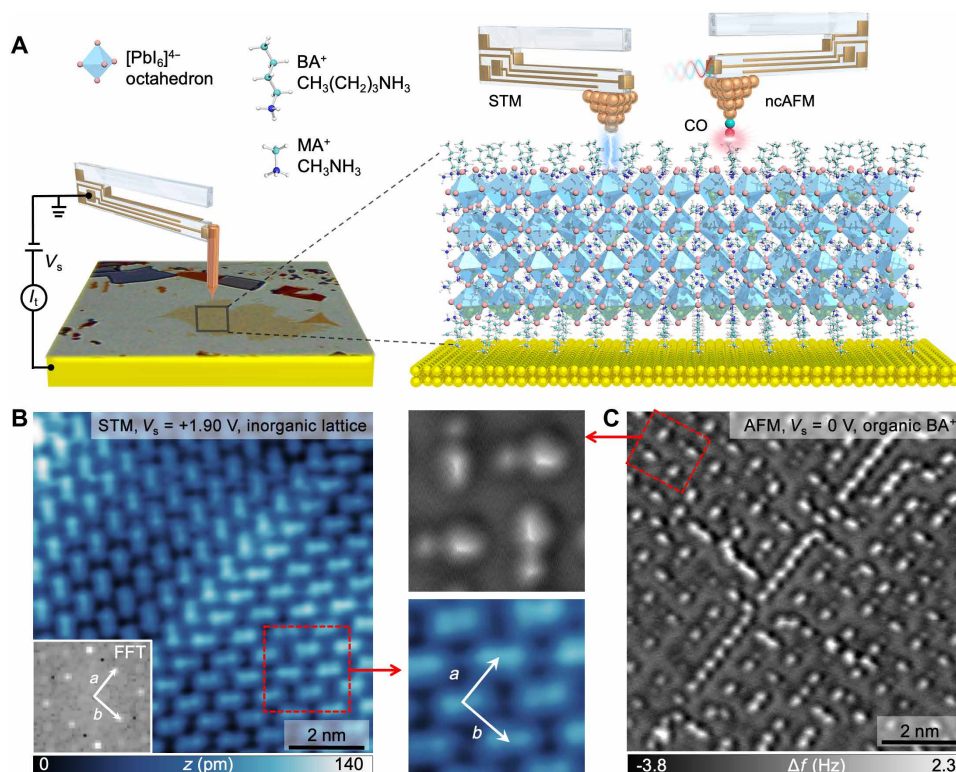
Fig. 1. qPlus-based STM and ncAFM imaging of the RPP surface. (**A**) Schematics showing a combined STM and ncAFM imaging of the RPP surface using a tuning fork–based qPlus sensor. Atomic layers of the RPP crystals are obtained by a mechanical exfoliation and then transferred onto the conducting Au substrate (optical image on the left). (**B**) STM image of RPP acquired at positive sample bias voltage ($V_s = +1.9$ V). (**C**) ncAFM image collected over the same surface area. ncAFM image was acquired in constant-height mode, at a tip-sample distance of $\Delta z = +100$ pm with respect to an original set point of $V_s = 2$ V and $I = 15$ pA.

resembles one acquired on the surfaces of 3D hybrid lead-halide perovskites, including MA^+PbBr_3 (34–36), MA^+PbI_3 (37–39), and $CsPbBr_3$ (40). The origin of each dimer has been ascribed to a pair of halogen atoms located at apices of neighboring $[PbI]_6$ octahedra, which are distorted owing to the ferroelectric-like organizations of the inner MA^+ cations (39). The simulated STM image of the $n = 4$ RPP structure also reproduces the dimer-like STM pattern observed experimentally (fig. S3). In addition, the calculated partial density of electronic states (PDOS) reveals that the conduction band (CB) of the RPP crystal consists of electronic states contributed by 6s Pb and 5p I without BA^+ cations (fig. S8 and note S4). Therefore, STM contrast acquired at a positive bias voltage is dominated by the topmost I atoms.

Analysis of the optimized DFT $n = 4$ RPP structure (fig. S3) reveals that I-dimer reconstruction is attributed to the characteristic distortion of the $[PbI]_6$ inorganic cages that is intimately steered by hydrogen bonding interactions with the inner MA^+, organized in a ferroelectric-like manner. Note that the exclusive existence of the dimer-like pattern in 2D RPP is in stark contrast to the case of 3D lead-halide perovskites, which also reveal the abundant zigzag-like STM patterns associated with antiferroelectric-like organizations of the inner MA^+ cations (39). Such a different behavior is presumably attributed to the peculiar 2D nature of the RPPs that favors the sole ferroelectric-like arrangement of the inner MA^+ chains, leading to the emergence of extended ferroelastic domains.

On the other hand, STM images acquired at negative bias voltages contain abundant fuzzy features, presumably due to instability in imaging of the organic cations (fig. S2). In contrast, such an instability is absent in the STM images taken at positive bias voltages, as tunneling current is mainly contributed by inorganic lattice. The calculated PDOS (fig. S8) shows that valence band has a predominant contribution of 5p I states with a nonnegligible contribution of the BA^+-induced states, which allows for the visualization of the on-surface BA^+ cations at negative sample bias voltages. Thus, we

attribute the instabilities to rearrangements of BA^+ cations induced during the tunneling process. Representative reorganizations of BA^+ chains are captured by a series of ncAFM and STM images acquired over the same surface area (fig. S1 and note S3), which will be discussed in detail later on. Moreover, repeated scanning of an identical surface area leads to disruption of the local arrangement of BA^+ molecules, leading to a highly disordered STM pattern at negative bias voltage (see fig. S2).

ncAFM measurements of the RPPs

To circumvent the challenge in the noninvasive imaging of the BA^+ layer, we used the constant-height ncAFM imaging with a CO-terminated tip that was prepared according to the procedure described in Materials and Methods. The frequency shift (Δf) contrast in the constant-height ncAFM images is associated with the spatial variation of electrostatic, dispersive, and repulsive forces acting between CO-terminated tip and BA^+ cations in the Pauli repulsion regime (31). To eliminate the possible perturbations of BA^+ chains by the tunneling process, the tip was repositioned (typically >50 nm) over the intact RPP sample area for the subsequent ncAFM imaging at zero bias voltage (see details in Materials and Methods).

A representative high-resolution ncAFM image of the RPP surface (Fig. 2A) reveals "arrow-like" features arranged in a square-shaped array (see the additional large-scale ncAFM images in fig. S2). Here, each arrow-like feature represents a pair of apical methyl ($-CH_3$) groups of the two adjacent BA^+ molecules (denoted as BA^+ pair). Combined with subsequent STM imaging acquired over the same sample area, the location of the adsorbed (on-surface) BA^+ cations with respect to the underlying octahedral $[PbI]^-$ lattice can be determined unambiguously. Superimposing the underlying inorganic lattice determined from the STM image (Fig. 2C) over the corresponding ncAFM image (Fig. 2B) reveals that BA^+ pairs are located in between apical I atoms and are aligned along the [100] and [001] directions of the $[PbI]^-$ lattice. These findings further underpin the
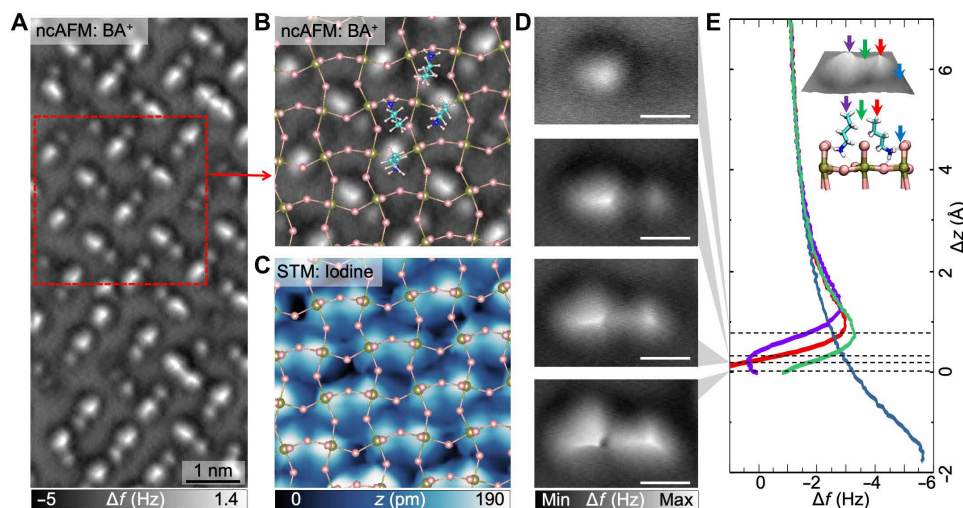
Fig. 2. The STM and ncAFM imaging of organic and inorganic layers in few-layer RPP. (**A**) Constant-height Δf image. (**B**) Zoom-in constant-height Δf image of the surface region marked by a red rectangle in (A). (**C**) STM image of the same surface area as shown in (B), superimposed with the structure of the DFT-relaxed RPP lattice. The color coding of elements: lead, green; iodine, pink; carbon, cyan; nitrogen, blue; and hydrogen, white. (**D**) A set of constant-height ncAFM images collected at various tip-sample distances (Δz) over an individual pair of BA^+ cations. (**E**) Δf versus Δz curves acquired over the sites marked by color-coded arrows in the experimental 3D-rendered ncAFM image in the inset (top) and side view of the DFT-relaxed BA^+ pair structure in the inset (bottom). The $\Delta z = 0$ is defined with respect to an STM set point of $V_s = 2$ V and $I = 15$ pA. Scale bars, 0.3 nm.

extraordinary capability of the combined STM/ncAFM measurements to unveil the geometry of both organic BA^+ arrays and the underlying inorganic octahedral lattice through noninvasive imaging of an RPP structure in a quasi-3D fashion.

To understand the ncAFM contrast of the BA^+ pairs associated with their peculiar conformations, we acquired frequency shift versus tip-sample distance $[(\Delta f(\Delta z)]$ curves over several characteristic sites (Fig. 2E), including over and between protruding methyl groups of the BA^+ chains, indicated by color-coded arrows in the inset of Fig. 2E. The $\Delta f(z)$ curves exhibit a minimum in the vicinity of $\Delta z \approx$ 1 Å, at which the attractive and repulsive tip-sample forces are balanced (41). The $\Delta f(\Delta z)$ curves measured over two paired BA^+ cations reveal a height variation of ~44 pm, estimated as the difference between the minima of the respective $\Delta f(z)$ curves. As shown in Fig. 2D, we also acquired a set of constant-height Δf images over an individual BA^+ pair at different tip-sample distances (also fig. S2, B to F). The constant-height Δf image taken at relatively large Δz shows a depression over the right BA^+ molecule due to an attractive tip-sample interaction. The left BA^+ chain has a larger surface protrusion of ~44 pm compared to the right BA^+ chain, leading to its brighter appearance arising from a stronger repulsive tip-sample interaction. A further decrease of Δz results in a gradual emergence of the sharp features associated with H atoms at -CH_3 groups of BA^+ molecules.

Mechanism of the BA+ pairing and BA+ interaction with I dimers

The aforementioned findings suggest that pairing of BA^+ cations and their cooperative periodic arrangement with respect to the octahedral $[PbI]^-$ lattice is likely driven by the short-range electrostatic interactions between the inorganic lattice and BA^+ cations. To gain a deeper insight into the origin of the unique arrangement of the BA^+ cations, we performed large-scale DFT + vdW calculations of RPP in the low-temperature orthorhombic configuration, which is typically adopted by $n = 4$ RPP below ~290 K (42, 43). The DFT-relaxed atomic structure (Fig. 3, D and E) reveals that the organic cations (MA^+ and BA^+) form electrostatic hydrogen-like bonds (denoted as H bonds) (44, 45) through their positively charged amine terminal groups (-NH_3) with the negatively charged I atoms from the inorganic cage. This interaction not only is responsible for the asymmetric arrangement of BA^+ molecules but also causes the structural deformation of the inorganic lattice, manifested by distortions of [PbI_6] cages in the xy plane and along the z axis (Fig. 3F). This also induces a significant surface relaxation of the organic cations, manifested by formation of the BA^+ pairs. In addition, the simulated CO-tip ncAFM images of the DFT-relaxed RPP model (Fig. 3, B and C) using the probe particle (denoted as PP) SPM model (46–48) reproduce the contrast observed in the experimental ncAFM images reasonably well (Fig. 3A). Furthermore, the PP-ncAFM images, simulated at various Δz (fig. S3), fully corroborate the experimental Δz-dependent evolution of the ncAFM contrast of BA^+ pairs (Fig. 2E), which further attests the validity of the uncovered atomic RPP structure.

The manipulation of BA+ pairs

Along with the aforementioned most abundant arrow-like conformation of BA^+ pairs (denoted as type I), ncAFM images also occasionally reveal the presence of another conformation type of BA^+ pairs, which assume a "Γ-like" form (denoted as type II). These conformations are interconvertible via STM imaging at elevated bias voltages. As
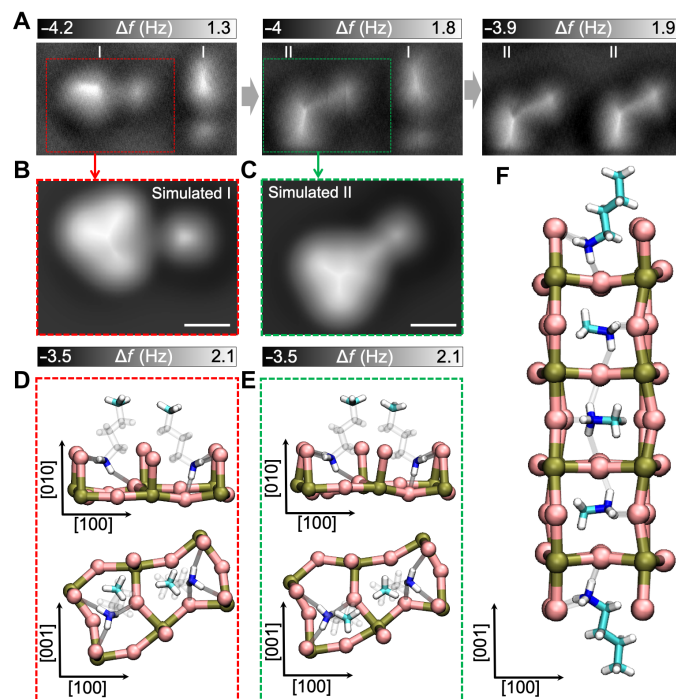
Fig. 3. Probing the origin of the pairing of the BA+ molecules. (**A**) ncAFM images of the same surface area showing the tip-assisted transformation of the BA^+ pairs from type I to type II. (**B**) Simulated ncAFM image of the "type I" BA^+ pair. (**C**) Simulated ncAFM image of the "type II" BA^+ pair. (**D**) The side and top view of the DFT-relaxed structure of the arrow-like type I BA^+ pair. (**E**) The side and top view of the DFT-relaxed structure of the Γ-like type II BA^+ pair. (**F**) The side view of the DFT-relaxed $n = 4$ RPP slab structure. The color coding of elements: lead, green; iodine, pink; carbon, cyan; nitrogen, blue; and hydrogen, white. Scale bars, 0.3 nm.

shown in Fig. 3A, a sequence of ncAFM images of the same surface area captures the tip-assisted transformation of BA^+ pairs, from type I to type II (additional data in fig. S4).

To investigate the mechanism behind the evolution of a BA^+ pair from type I to type II configuration, we performed a computational search for the other possible configurations of BA^+ molecules. We found another stable configuration (Fig. 3E), which differs in the total energy only by tens of milli–electron volts with respect to the original type I configuration. One BA^+ cation in this new configuration (i.e., type II) preserves its position, while the upper part of another BA^+ cation tilts along the [100] axis. The corresponding simulated PP-ncAFM image of this new configuration (Fig. 3C) also matches well to the experimental one. Throughout this transformation, an inorganic cage shows a negligible distortion because the amine groups of the BA^+ chains remain at their original locations via H-bonding with I atoms. Thus, applying bias voltage accompanied by the tunneling process locally modifies the orientation of BA^+ chains, without disruption of the ionic lattice. Note that our experimental ncAFM data reveal that the type I (arrow-like) BA^+ pair is the most frequently observed configuration (see fig. S7), while the type II (Γ-like) configuration is less abundant, suggesting that the type I configuration is energetically more favorable.

Origin of the twin-domain composition of the RPP crystal

Our large-scale STM imaging unambiguously reveals that the orthorhombic RPP structure exclusively consists of the alternating

ferroelastic (*49*) domains (color-coded as green and red in Fig. 4A) and twin boundaries, which are nearly parallel-aligned along the [100] direction. The I dimers in adjacent ferroelastic domains are found to be orientated along the [101] and [10−1] lattice directions. Each ferroelastic domain is rendered by cooperative ferroelectric-like alignment of the inner MA^+ dipoles as denoted schematically by blue-red arrows in Fig. 4F (also fig. S3). Specifically, on the basis of the fact that $n = 4$ RPP hosts an odd number of MA^+ layers (three), the individual RPP domain is expected to attain a net nonzero polarization associated with the cooperative alignment of the MA^+ chains within each octahedral sheet. Therefore, twin boundaries linked to the intrinsic orthorhombic structure of RPP emerge at the borders of the neighboring ferroelastic domains with opposite orientation of the net MA^+ dipole moments. The twin-domain composition of the RPP crystalline flakes, with quasi-1D twin boundaries extended over hundreds of nanometers, has not been reported to date. Despite the observation of twin-domain boundaries in 3D MA^+PbI_3 films using x-ray diffraction, TEM, and piezoresponse force microscopy

imaging techniques (*49–53*), neither one reveals the formation of extended quasi-1D twin boundaries, as observed in 2D RPP.

Such a twin-domain composition of the RPP consists of two types of domain boundaries, namely, "head-to-head" (ammonium-to-ammonium) (Fig. 4B) and "tail-to-tail" (methyl-to-methyl) (Fig. 4D), which were predicted to host positive and negative electrostatic potential, respectively (*54*, *55*). To verify this hypothesis, we conducted Kelvin probe force microscopy (KPFM) measurements (see Materials and Methods and note S3) to probe the local contact potential difference (LCPD), which can be associated with the spatial variation of the local work function (*56*) across the domain walls. LCPD maps unambiguously show a lower and higher LCPD value over head-to-head (Fig. 4C) and tail-to-tail (Fig. 4E) twin boundaries, respectively.

Such a characteristic LCPD variation across the twin boundaries has been consistently observed by multiple sessions of KPFM measurements, which suggest the presence of a positive (negative) electrostatic potential in the vicinity of head-to-head (tail-to-tail) twin boundaries. It needs to be noted that absolute magnitude of the LCPD contrast does not reflect the magnitude of the electrostatic potential, because the CPD value strongly depends on the structure of tip apex and KPFM acquisition set point (*56*). To illustrate this, we present KPFM measurements acquired using the same tip apex at varying tip-sample distances in fig. S6, which reveals a remarkable change of the CPD value upon a decrease of the tip-sample distance.

The contrast of LCPD maps (Fig. 4, C and E) is in good agreement with the landscape of the electrostatic potential over head-to-head (tail-to-tail) twin boundaries calculated for a twin boundaries slab model depicted in Fig. 4F. Here, to decipher the origin of the LCPD signal across the domain boundaries, we designed the slab model consisting of 3600 atoms including both types of twin boundaries separated by a buffer level ensuring sufficient separation of the twin boundaries. We carried out large-scale total energy DFT-vdW calculations to obtain the fully optimized atomic structure of $n = 4$ RPP. We then calculated individual dipole moments of individual BA^+ and MA^+ molecules for constructing an effective lattice dipole model (see note S4 for more details). This model allows us to decipher the impact of the individual molecular BA^+ and MA^+ layers on the resulting electrostatic potential. We found that the outermost MA^+ molecular layer plays a decisive role on the character of the electrostatic potential across the domain walls.

We note that the intrinsic ferroelastic-like composition of the 2D RPP crystals, uncovered by our STM/ncAFM studies, can be a key toward understanding their outstanding photovoltaic characteristics and the occurrence of a number of intriguing optical properties unveiled recently (*17–22*). Specifically, recent temperature-dependent PL studies reveal an emergence of shallow electronic states in the $n = 4$ $(BA^+)_2(MA^+)_{n-1}Pb_nI_{3n+1}$ RPP with an increased emission lifetime. These electronic states were previously ascribed to the presence of local domains and static disorder in the crystal that emerged at low temperature (*22*), although their structure has not been verified. Our findings not only provide a new quantitative insight into nanoscale domain composition of the RPPs but also suggest that low-energy electronic states revealed by PL spectra are likely associated with the domain structures observed here.

Furthermore, the polarized electrostatic potential across twin boundaries, revealed by our KPFM studies and corroborated by DFT calculations, is expected to facilitate the separation of electron-hole pairs at head-to-head and tail-to-tail twin boundaries hosting opposite electrostatic potential, thus leading to reduced rates of
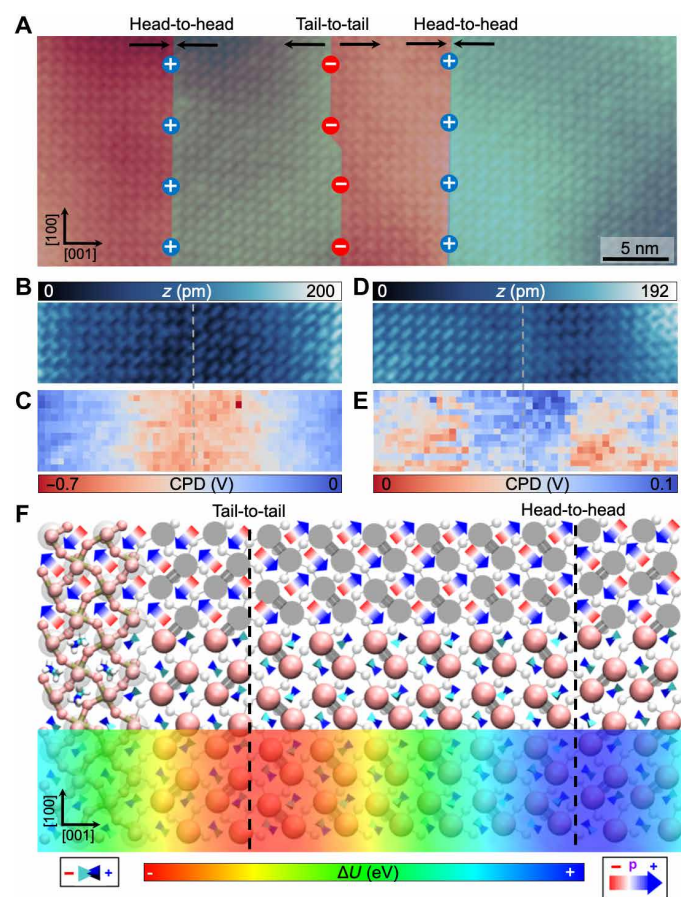
Fig. 4. Imaging the domain structure and electrostatic potential across the twin-domain boundary. (**A**) Large-scale STM image of the RPPs reveals a twin-domain crystal composition. Distinct ferroelastic domains are color-coded by blue and red. (**B** and **C**) STM image (B) and the corresponding 2D LCPD map (C) of the head-to-head twin boundary. (**D** and **E**) STM image (D) and the corresponding LCPD map (E) of the tail-to-tail twin boundary. (**F**) The DFT-relaxed structure of the head-to-head and tail-to-tail twin boundaries, superimposed with a surface electrostatic potential determined using a lattice dipole model. Red-blue color-coded arrows represent dipole moments associated with MA^+ chains.

electron-hole recombination in RPPs. Analogous to this, the separation of electron and hole pairs at ferroelastic domain boundaries has been proposed to result in a reduced rate of exciton recombination in 3D hybrid perovskites (57–59). However, the electrostatic potential of these domain boundaries has not been quantitatively probed to date.

Last, owing to their one-dimensional nature (hundreds of nanometers), twin boundaries can be viewed as channels for a long-distance exciton propagation, which is directly corroborated by a recently reported phenomenon of the long-range (hundreds of nanometers) exciton funneling in RPPs (18, 19, 22). It is therefore envisaged that controlling the orientation of the twin boundaries via external stimuli (17, 60, 61) can be a plausible strategy to enhance the performance of the RPP-based photovoltaic and optoelectronic devices.

DISCUSSION
We have deployed STM and tip-functionalized ncAFM techniques for a precise identification of the low temperature ground state configuration of a prototypical RPP hybrid perovskite, providing real-space picture of microstructures for a better understanding of LT optical properties in RPPs. In particular, the STM imaging resolves the dimer-like atomic reconstruction of the underlying inorganic lead-halide lattice, whereas ncAFM measurement with a CO-tip allows visualization of the cooperative ordering of on-surface BA^+ cation pairs. Corroborated by DFT calculations, joint STM/ncAFM measurements not only enable gaining detailed insight into hydrogen-like interactions between organic cations and inorganic lattice but also point to a high degree of flexibility of inorganic framework strongly affecting the organic cations even at low temperature. On-surface structural relaxation of BA^+ cations observed here may have a larger impact on macroscopic physical properties of RPP flakes with reduced thickness. The molecular softness of RPPs with the cooperative lattice relaxation allows for strain-tunable optical properties of atomically thin RPP flakes (17).

In addition, combined STM/ncAFM measurements also reveal the existence of domains in the RPP crystal, which arise from the cooperative alignment of interior polar MA^+ chains and a synergetic distortion of the $[PbI]^-$ lattice. We note that the ferroelastic domain composition of RPP has recently been reported using a polarized optical microscope under external strain (62). Nevertheless, this work provides details of the atomic structures and electrostatic potential distribution across the twin domain. It is envisaged that existence of extended charged domain boundaries may have several implications for the optoelectronic performance of thin 2D perovskite films. First, alternating distribution of the electrostatic potential across domain boundaries may facilitate the separation of electron-hole pairs and thus lead to reduced rates of electron-hole recombination (57–59). Second, spatially extended one-dimensional twin boundaries (hundreds of nanometers) can be responsible for the long-range exciton funneling in RPPs as reported recently (18, 19, 22).

To date, the tip-functionalized ncAFM technique has been mostly used for imaging of molecular structures (31), artificial weakly bonded systems (32, 33), and layered inorganic materials (63, 64). Our work underpins tremendous potential of this technique, for a noninvasive imaging of a wide range of soft organic-inorganic hybrid functional materials with diverse organic spacers (4) beyond lead-halide RPPs. In addition, a synergetic combination of the STM, ncAFM, and

KPFM studies with in situ external stimuli (e.g., light irradiation or electric field) allows one to gain a deeper microscopic insight into technologically relevant optoelectronic phenomena in these materials including lattice relaxation and associated polaronic effects, ion migration, and emergence of ferroelectricity (2, 6, 11).

MATERIALS AND METHODS
Sample preparation
The RPP single crystals were synthesized using three solid precursors—PbO, $C_4H_9NH_3I$, and CH_3NH_3I—via a temperature-programmed solution precipitation method, described in detail in our recent report (17). The phase purity and elemental constitution of RPP crystals were confirmed using x-ray diffraction and PL measurements (17). Thin RPP flakes were obtained via mechanical exfoliation of bulk crystals in the inert glove-box environment and then transferred onto the flat Au(100) surface for STM/ncAFM measurements. The Au(100)-supported RPP flakes were immediately transferred to the load-lock chamber of our SPM system held at a base pressure better than 1×10^{-6} mbar. The transfer process involved very limited air exposure (typically 1 to 2 min) of RPP flakes. Single-crystal Au(100) is chosen as the support owing to its surface flatness and ability to offer a suitable optical contrast of few-layered RPP flakes that facilitate tip allocation.

The qPlus STM/ncAFM measurements
The STM and ncAFM experiments were performed under ultrahigh vacuum conditions at 4.4 K using a commercial Omicron LT STM/AFM machine. We used a qPlus sensor with a resonant frequency of $f_0 = 28.5$ kHz, a quality factor of $Q = 12000$, and an oscillation amplitude of $A = 100$ to 120 pm, operated in frequency-modulation mode. All ncAFM images were collected in constant-height mode. Stabilization parameters before feedback loop opening are indicated in the corresponding figure captions.

We used chemically etched tungsten tips that were treated by repeated gentle indentations (~1 to 2 nm) into a clean Cu(111) surface, followed by the application of voltage pulses. The clean and sharp tip was functionalized by picking up an individual CO molecule, dosed at low temperature (~7 K) onto the Cu(111) surface. The routine CO-functionalization procedure involves parking tip over an individual CO molecule ($V_s = 1$ V and $I = 1$ nA), followed by opening a feedback loop and ramping V_s to the range from 2.7 to 3 V for 20 to 30 s until the occurrence of a sharp drop in the $I(t)$ channel—a fingerprint of a successful CO transfer onto the tip apex.

Typically, the CO-functionalized tip was engaged with the RPP surface in constant-current mode (set point: $V_s = +2.3$ V; $I = 10$ pA), which unavoidably perturbed the proximate BA^+ chains. To probe the "fully unperturbed" BA^+ reconstruction, we routinely repositioned the tip away (~50 nm) from the engaging point and subsequently probed the new intact RPP area in constant-height ncAFM imaging mode. We applied zero bias voltage during tip repositioning and ncAFM imaging to avoid any possible perturbations of BA^+ chains triggered by the tunneling process.

KPFM mapping measurements
Kelvin parabolas were acquired in a (50×12 pixel) grid covering head-to-head and tail-to-tail domain boundaries, with an acquisition time of 30 s per pixel. The V_{CPD} values were further extracted from each Kelvin parabola via parabolic fit using the formula

$\Delta f(V) = a(V_s - V_{CPD})2 + c$ (see note S3 for further details). These V_{CPD} values were used to construct the 2D LCPD maps as shown in Fig. 4 (C and E).

Computational methods

The DFT calculations were performed using the Fireball package (*65*). All geometry optimizations and electronic structure analyses were performed using the BLYP exchange-correlation functional (*66*, *67*) with D3 corrections (*68*) and norm-conserving pseudopotentials with a basis set of optimized numerical atomic-like orbitals (*69*). Systems were allowed to relax until the remaining atomic forces reached below 5×10^{-2} eV Å^{-1}. Two slabs were used in this study: (i) a 2×2 unit cell containing 300 atoms and (ii) a specifically designed slab mimicking the domain boundaries with 3600 atoms in total. The Brillouin reciprocal zone was sampled by a Monkhorst-Pack grid of $5 \times 5 \times 1$ for the 2×2 slab and 1 k-point for the large domain boundaries slab. The theoretical AFM simulations were carried out using the probe particle SPM code (*46*–*48*), with the Hartree potential obtained from the DFT calculations, with a probe particle stiffness of $k = 0.7$ N/m and $R_c = 1.661$ Å to simulate the CO-functionalized tip.

SUPPLEMENTARY MATERIALS

REFERENCES AND NOTES

1. G. Grancini, M. K. Nazeeruddin, Dimensional tailoring of hybrid perovskites for photovoltaics. *Nat. Rev. Mater.* **4**, 4–22 (2019).
2. K. Leng, W. Fu, Y. Liu, M. Chhowalla, K. P. Loh, From bulk to molecularly thin hybrid perovskites. *Nat. Rev. Mater.* **5**, 482–500 (2020).
3. L. Dou, A. B. Wong, Y. Yu, M. Lai, N. Kornienko, S. W. Eaton, A. Fu, C. G. Bischak, J. Ma, T. Ding, N. S. Ginsberg, L. W. Wang, A. P. Alivisatos, P. Yang, Atomically thin two-dimensional organic-inorganic hybrid perovskites. *Science* **349**, 1518–1521 (2015).
4. M. D. Smith, E. J. Crace, A. Jaffe, H. I. Karunadasa, The diversity of layered halide perovskites. *Annu. Rev. Mat. Res.* **48**, 111–136 (2018).
5. I. C. Smith, E. T. Hoke, D. Solis-Ibarra, M. D. McGehee, H. I. Karunadasa, A layered hybrid perovskite solar-cell absorber with enhanced moisture stability. *Angew. Chem. Int. Ed.* **126**, 11414–11417 (2014).
6. C. Katan, N. Mercier, J. Even, Quantum and dielectric confinement effects in lower-dimensional hybrid perovskite semiconductors. *Chem. Rev.* **119**, 3140–3192 (2019).
7. R. L. Milot, R. J. Sutton, G. E. Eperon, A. A. Haghighirad, J. Martinez Hardigree, L. Miranda, H. J. Snaith, M. B. Johnston, L. M. Herz, Charge-carrier dynamics in 2D hybrid metal–halide perovskites. *Nano Lett.* **16**, 7001–7007 (2016).
8. J.-C. Blancon, A. V. Stier, H. Tsai, W. Nie, C. C. Stoumpos, B. Traoré, L. Pedesseau, M. Kepenekian, F. Katsutani, G. T. Noe, J. Kono, S. Tretiak, S. A. Crooker, C. Katan, M. G. Kanatzidis, J. J. Crochet, J. Even, A. D. Mohite, Scaling law for excitons in 2D perovskite quantum wells. *Nat. Commun.* **9**, 2254 (2018).
9. P. Gao, A. R. B. M. Yusoff, M. K. Nazeeruddin, Dimensionality engineering of hybrid halide perovskite light absorbers. *Nat. Commun.* **9**, 5028 (2018).
10. I. Abdelwahab, P. Dichtl, G. Grinblat, K. Leng, X. Chi, I.-H. Park, M. P. Nielsen, R. F. Oulton, K. P. Loh, S. A. Maier, Giant and tunable optical nonlinearity in single-crystalline 2D perovskites due to excitonic and plasma effects. *Adv. Mater.* **31**, 1902685 (2019).
11. Y. Chen, Y. Sun, J. Peng, J. Tang, K. Zheng, Z. Liang, 2D Ruddlesden-Popper perovskites for optoelectronics. *Adv. Mater.* **30**, 1703487 (2018).
12. D. H. Cao, C. C. Stoumpos, O. K. Farha, J. T. Hupp, M. G. Kanatzidis, 2D Homologous perovskites as light-absorbing materials for solar cell applications. *J. Am. Chem. Soc.* **137**, 7843–7850 (2015).
13. P. Cui, D. Wei, J. Ji, H. Huang, E. Jia, S. Dou, T. Wang, W. Wang, M. Li, Planar p–n homojunction perovskite solar cells with efficiency exceeding 21.3%. *Nature Energy* **4**, 150–159 (2019).
14. H. Tsai, W. Nie, J. C. Blancon, C. C. Stoumpos, R. Asadpour, B. Harutyunyan, A. J. Neukirch, R. Verduzco, J. J. Crochet, S. Tretiak, L. Pedesseau, J. Even, M. A. Alam, G. Gupta, J. Lou, P. M. Ajayan, M. J. Bedzyk, M. G. Kanatzidis, A. D. Mohite, High-efficiency two-dimensional Ruddlesden-Popper perovskite solar cells. *Nature* **536**, 312–316 (2016).
15. E. Shi, B. Yuan, S. B. Shiring, Y. Gao, Akriti, Y. Guo, C. Su, M. Lai, P. Yang, J. Kong, B. M. Savoie, Y. Yu, L. Dou, Two-dimensional halide perovskite lateral epitaxial heterostructures. *Nature* **580**, 614–620 (2020).
16. D. Pan, Y. Fu, N. Spitha, Y. Zhao, C. R. Roy, D. J. Morrow, D. D. Kohler, J. C. Wright, S. Jin, Deterministic fabrication of arbitrary vertical heterostructures of two-dimensional Ruddlesden-Popper halide perovskites. *Nat. Nanotechnol.* **16**, 159–165 (2021).
17. K. Leng, I. Abdelwahab, I. Verzhbitskiy, M. Telychko, L. Chu, W. Fu, X. Chi, N. Guo, Z. Chen, Z. Chen, C. Zhang, Q.-H. Xu, J. Lu, M. Chhowalla, G. Eda, K. P. Loh, Molecularly thin two-dimensional hybrid perovskites with tunable optoelectronic properties due to reversible surface relaxation. *Nat. Mater.* **17**, 908–914 (2018).
18. S. Deng, E. Shi, L. Yuan, L. Jin, L. Dou, L. Huang, Long-range exciton transport and slow annihilation in two-dimensional hybrid perovskites. *Nat. Commun.* **11**, 664 (2020).
19. M. Seitz, A. J. Magdaleno, N. Alcázar-Cano, M. Meléndez, T. J. Lubbers, S. W. Walraven, S. Pakdel, E. Prada, R. Delgado-Buscalioni, F. Prins, Exciton diffusion in two-dimensional metal-halide perovskites. *Nat. Commun.* **11**, 2035 (2020).
20. D. B. Straus, C. R. Kagan, Electrons, excitons, and phonons in two-dimensional hybrid perovskites: Connecting structural, optical, and electronic properties. *J. Phys. Chem. Lett.* **9**, 1434–1447 (2018).
21. C. M. Mauck, W. A. Tisdale, Excitons in 2D organic–inorganic halide perovskites. *Trends Chem.* **1**, 380–393 (2019).
22. A. Baldwin, G. Delport, K. Leng, R. Chahbazian, K. Galkowski, K. P. Loh, S. D. Stranks, Local energy landscape drives long-range exciton diffusion in two-dimensional halide perovskite semiconductors. *J. Phys. Chem. Lett.* **12**, 4003–4011 (2021).
23. M. U. Rothmann, J. S. Kim, J. Borchert, K. B. Lohmann, C. M. O'Leary, A. A. Sheader, L. Clark, H. J. Snaith, M. B. Johnston, P. D. Nellist, L. M. Herz, Atomic-scale microstructure of metal halide perovskite. *Science* **370**, eabb5940 (2020).
24. D. Zhang, Y. Zhu, L. Liu, X. Ying, C.-E. Hsiung, R. Sougrat, K. Li, Y. Han, Atomic-resolution transmission electron microscopy of electron beam-sensitive crystalline materials. *Science* **359**, 675–679 (2018).
25. Z. Yuanyuan, H. Sternlicht, N. P. Padture, Transmission electron microscopy of halide perovskite materials and devices. *Joule* **3**, 641–661 (2019).
26. S. Chen, P. Gao, Challenges, myths, and opportunities of electron microscopy on halide perovskites. *J. App. Phys.* **128**, 010901 (2020).
27. F. J. Giessibl, The Qplus sensor, a powerful core for the atomic force microscope. *Rev. Sci. Instrum.* **90**, 011101 (2019).
28. H. Labidi, M. Koleini, T. Huff, M. Salomons, M. Cloutier, J. Pitters, R. A. Wolkow, Indications of chemical bond contrast in AFM images of a hydrogen-terminated silicon surface. *Nat. Commun.* **8**, 14222 (2017).
29. L. Gross, F. Mohn, N. Moll, P. Liljeroth, G. Meyer, The chemical structure of a molecule resolved by atomic force microscopy. *Science* **325**, 1110–1114 (2009).
30. D. G. de Oteyza, P. Gorman, Y.-C. Chen, S. Wickenburg, A. Riss, D. J. Mowbray, G. Etkin, Z. Pedramrazi, H.-Z. Tsai, A. Rubio, M. F. Crommie, F. R. Fischer, Direct imaging of covalent bond structure in single-molecule chemical reactions. *Science* **340**, 1434–1437 (2013).
31. P. Jelínek, High resolution SPM imaging of organic molecules with functionalized tips. *J. Phys.-Condens. Mat.* **29**, 343002 (2017).
32. J. Peng, J. Guo, P. Hapala, D. Cao, R. Ma, B. Cheng, L. Xu, M. Ondráček, P. Jelínek, E. Wang, Y. Jiang, Weakly perturbative imaging of interfacial water with submolecular resolution by atomic force microscopy. *Nat. Commun.* **9**, 122 (2018).
33. A. Shiotari, Y. Sugimoto, Ultrahigh-resolution imaging of water networks by atomic force microscopy. *Nat. Commun.* **8**, 14313 (2017).
34. H.-C. Hsu, B.-C. Huang, S.-C. Chin, C.-R. Hsing, D.-L. Nguyen, M. Schnedler, R. Sankar, R. E. Dunin-Borkowski, C.-M. Wei, C.-W. Chen, P. Ebert, Y.-P. Chiu, Photodriven dipole reordering: Key to carrier separation in metalorganic halide perovskites. *ACS Nano* **13**, 4402–4409 (2019).
35. J. Hieulle, X. Wang, C. Stecker, D.-Y. Son, L. Qiu, L. R. Ohmann, L. K. Ono, A. Mugarza, Y. Yan, Y. Qi, Unraveling the impact of halide mixing on perovskite stability. *J. Am. Chem. Soc.* **141**, 3515–3523 (2019).
36. C. Stecker, K. Liu, J. Hieulle, R. Ohmann, Z. Liu, L. K. Ono, G. Wang, Y. Qi, Surface defect dynamics in organic–inorganic hybrid perovskites: From mechanism to interfacial properties. *ACS Nano* **13**, 12127–12136 (2019).
37. L. She, M. Liu, X. Li, Z. Cai, D. Zhong, Growth and interfacial structure of methylammonium lead iodide thin films on Au(111). *Surf. Sci.* **656**, 17–23 (2017).
38. L. She, M. Liu, D. Zhong, Atomic structures of $CH_3NH_3PbI_3$ (001) surfaces. *ACS Nano* **10**, 1126–1131 (2016).
39. R. Ohmann, L. K. Ono, H.-S. Kim, H. Lin, M. V. Lee, Y. Li, N.-G. Park, Y. Qi, Real-space imaging of the atomic structure of organic–inorganic perovskite. *J. Am. Chem. Soc.* **137**, 16049–16054 (2015).
40. J. Hieulle, S. Luo, D.-Y. Son, A. Jamshaid, C. Stecker, Z. Liu, G. Na, D. Yang, R. Ohmann, L. K. Ono, L. Zhang, Y. Qi, Imaging the atomic structure of all-inorganic halide perovskites. *J. Phys. Chem. Lett.* **11**, 818–823 (2020).

41. N. J. Heijden, P. Hapala, J. A. Rombouts, J. Lit, D. Smith, P. Mutombo, M. Švec, P. Jelínek, I. Swart, Characteristic contrast in Δf_{min} maps of organic molecules using atomic force microscopy. *ACS Nano* **10**, 8517–8525 (2016).

42. C. C. Stoumpos, D. H. Cao, D. J. Clark, J. Young, J. M. Rondinelli, J. I. Jang, J. T. Hupp, M. G. Kanatzidis, Ruddlesden-Popper hybrid lead iodide perovskite 2D homologous semiconductors. *Chem. Mater.* **28**, 2852–2867 (2016).

43. D. G. Billing, A. Lemmerer, Synthesis, characterization and phase transitions in the inorganic–organic layered perovskite-type hybrids [(C$_n$H$_{2n+1}$NH$_3$)$_2$PbI$_4$], n = 4, 5 and 6. *Acta Crystallogr.* **63**, 735–747 (2007).

44. A. M. A. Leguy, J. M. Frost, A. P. McMahon, V. G. Sakai, W. Kockelmann, C. H. Law, X. Li, F. Foglia, A. Walsh, B. C. O'Regan, J. Nelson, J. T. Cabral, P. R. F. Barnes, The dynamics of methylammonium ions in hybrid organic–inorganic perovskite solar cells. *Nat. Commun.* **6**, 7124 (2015).

45. C. Motta, F. El-Mellouhi, S. Kais, N. Tabet, F. Alharbi, S. Sanvito, Revealing the role of organic cations in hybrid halide perovskite CH$_3$NH$_3$PbI$_3$. *Nat. Commun.* **6**, 7026 (2014).

46. P. Hapala, G. Kichin, C. Wagner, F. Stefan Tautz, R. Temirov, P. Jelínek, Mechanism of high-resolution STM/AFM imaging with functionalized tips. *Phys. Rev. B* **90**, 085421 (2014).

47. O. Krejčí, P. Hapala, M. Ondráček, P. Jelínek, Principles and simulations of high-resolution STM imaging with a flexible tip apex. *Phys. Rev. B* **95**, 045407 (2017).

48. P. Hapala, R. Temirov, F. S. Tautz, P. Jelínek, Origin of high-resolution IETS-STM images of organic molecules with functionalized tips. *Phys. Rev. Lett.* **113**, 226101 (2014).

49. Y. Liu, L. Collins, R. Proksch, S. Kim, B. R. Watson, B. Doughty, T. R. Calhoun, M. Ahmadi, A. V. Ievlev, S. Jesse, S. T. Retterer, A. Belianinov, K. Xiao, J. Huang, B. G. Sumpter, S. V. Kalinin, B. Hu, O. S. Ovchinnikova, Chemical nature of ferroelastic twin domains in CH$_3$NH$_3$PbI$_3$ perovskite. *Nat. Mater.* **17**, 1013–1019 (2018).

50. F. Bertolotti, L. Protesescu, M. V. Kovalenko, S. Yakunin, A. Cervellino, S. J. L. Billinge, M. W. Terban, J. S. Pedersen, N. Masciocchi, A. Guagliardi, Coherent nanotwins and dynamic disorder in cesium lead halide perovskite nanocrystals. *ACS Nano* **11**, 3819–3831 (2017).

51. I. M. Hermes, S. A. Bretschneider, V. W. Bergmann, D. Li, A. Klasen, J. Mars, W. Tremel, F. Laquai, H. J. Butt, M. Mezger, R. Berger, B. J. Rodriguez, S. A. L. Weber, Ferroelastic fingerprints in methylammonium lead iodide perovskite. *J. Phys. Chem. C* **120**, 5724–5731 (2016).

52. Y. Kutes, Y. L. Ye, Y. Zhou, S. Pang, B. D. Huey, N. P. Padture, Direct observation of ferroelectric domains in solution-processed CH$_3$NH$_3$PbI$_3$ perovskite thin films. *J. Phys. Chem. Lett.* **5**, 3335–3339 (2014).

53. M. U. Rothmann, W. Li, Y. Zhu, Y. Bach, L. Spiccia, J. Etheridge, Y.-B. Cheng, Direct observation of intrinsic twin domains in tetragonal CH$_3$NH$_3$PbI$_3$. *Nat. Commun.* **8**, 14547 (2017).

54. A. R. Warwick, J. Íñiguez, P. D. Haynes, N. C. Bristowe, First-principles study of ferroelastic twins in halide perovskites. *J. Phys. Chem. Lett.* **10**, 1416–1421 (2019).

55. S. Liu, F. Zheng, N. Z. Koocher, H. Takenaka, F. Wang, A. M. Rappe, Ferroelectric domain wall induced band gap reduction and charge separation in organometal halide perovskites. *J. Phys. Chem. Lett.* **6**, 693–699 (2015).

56. W. Melitz, J. Shen, A. C. Kummel, S. Lee, Kelvin probe force microscopy and its application. *Surf. Sci. Rep.* **66**, 1–27 (2011).

57. T. S. Sherkar, L. Jan Anton Koster, Can ferroelectric polarization explain the high performance of hybrid halide perovskite solar cells? *Phys. Chem. Chem. Phys.* **18**, 331–338 (2015).

58. F. Bi, S. Markov, R. Wang, Y. H. Kwok, W. Zhou, L. Liu, X. Zheng, G. H. Chen, C. Y. Yam, Enhanced photovoltaic properties induced by ferroelectric domain structures in organometallic halide perovskites. *J. Phys. Chem. C* **121**, 11151–11158 (2017).

59. J. M. Frost, K. T. Butler, F. Brivio, C. H. Hendon, M. Schilfgaarde, A. Walsh, Atomistic origins of high-performance in hybrid halide perovskite solar cells. *Nano Lett.* **14**, 2584–2590 (2014).

60. Y. Li, M. Behtash, J. Wong, K. Yang, Enhancing ferroelectric dipole ordering in organic–inorganic hybrid perovskite CH$_3$NH$_3$PbI$_3$: Strain and doping engineering. *J. Phys. Chem. C* **122**, 177–184 (2018).

61. T. W. Jones, A. Osherov, M. Alsari, M. Sponseller, B. C. Duck, Y. K. Jung, C. Settens, F. Niroui, R. Brenes, C. V. Stan, Y. Li, M. Abdi-Jalebi, N. Tamura, J. E. Macdonald, M. Burghammer, R. H. Friend, V. Bulović, A. Walsh, G. J. Wilson, S. Lilliu, S. D. Stranks, Lattice strain causes non-radiative losses in halide perovskites. *Energy Environ. Sci.* **12**, 596–606 (2019).

62. X. Xiao, J. Zhou, K. Song, J. Zhao, Y. Zhou, P. N. Rudd, Y. Han, J. Li, J. Huang, Layer number dependent ferroelasticity in 2D Ruddlesden–Popper organic-inorganic hybrid perovskites. *Nat Commun.* **12**, 1332 (2021).

63. B. Schuler, D. Y. Qiu, S. Refaely-Abramson, C. Kastl, C. T. Chen, S. Barja, R. J. Koch, D. F. Ogletree, S. Aloni, A. M. Schwartzberg, J. B. Neaton, S. G. Louie, A. Weber-Bargioni, Large spin-orbit splitting of deep in-gap defect states of engineered sulfur vacancies in monolayer WS$_2$. *Phys. Rev. Lett.* **123**, 076801 (2019).

64. F. Schulz, J. Ritala, O. Krejčí, A. P. Seitsonen, A. S. Foster, P. Liljeroth, Elemental identification by combining atomic force microscopy and Kelvin probe force microscopy. *ACS Nano* **12**, 5274–5283 (2018).

65. J. P. Lewis, P. Jelínek, J. Ortega, A. A. Demkov, D. G. Trabada, B. Haycock, H. Wang, G. Adams, J. K. Tomfohr, E. Abad, H. Wang, D. A. Drabold, Advances and applications in the FIREBALL ab initio tight-binding molecular-dynamics formalism. *Phys. Status Solidi B.* **248**, 1989–2007 (2011).

66. A. D. Becke, Density-functional exchange-energy approximation with correct asymptotic behavior. *Phys. Rev. A* **38**, 3098–3100 (1988).

67. C. Lee, W. Yang, R. G. Parr, Development of the Colle-Salvetti correlation-energy formula into a functional of the electron density. *Phys. Rev. B* **37**, 785–789 (1988).

68. S. Grimme, S. Ehrlich, L. Goerigk, Effect of the damping function in dispersion corrected density functional theory. *J. Comput. Chem.* **32**, 1456–1465 (2011).

69. M. A. Basanta, Y. J. Dappe, P. Jelínek, J. Ortega, Optimized atomic-like orbitals for first-principles tight-binding molecular dynamics. *J. Comput. Mater. Sci.* **39**, 759–766 (2007).

70. K. Leng, L. Wang, Y. Shao, I. Abdelwahab, G. Grinblat, I. Verzhbitskiy, R. Li, Y. Cai, X. Chi, W. Fu, P. Song, A. Rusydi, G. Eda, S. A. Maier, K. P. Loh, Electron tunneling at the molecularly thin 2D perovskite and graphene van der Waals interface. *Nat. Commun.* **11**, 5483 (2020).

71. L. Gross, F. Mohn, P. Liljeroth, J. Repp, F. Giessibl, G. Meyer, Measuring the charge state of an adatom with noncontact atomic force microscopy. *Science* **324**, 1428–1431 (2009).

ScienceAdvances

Sub-angstrom noninvasive imaging of atomic arrangement in 2D hybrid perovskites

Mykola TelychkoShayan EdalatmaneshKai LengIbrahim AbdelwahabNa GuoChun ZhangJesús I. Mendieta-MorenoMatyas NachtigallJing LiKian Ping LohPavel JelínekJiong Lu

View the article online
https://www.science.org/doi/10.1126/sciadv.abj0395
Permissions
https://www.science.org/help/reprints-and-permissions

Use of this article is subject to the Terms of service